Communications in Physics, Vol. 28, No. 2 (2018), pp. 97-114
DOI:10.15625/0868-3166/28/2/12595

Review paper

COHERENT DIFFRACTIVE IMAGING USING TABLE-TOP HIGH HARMONIC GENERATION

KHUONG BA DINH[a,b],[†], KHOA ANH TRAN[a], PETER HANNAFORD[a]
AND LAP VAN DAO[a]

[a]*Centre for Quantum and Optical Science, Swinburne University of Technology, Melbourne, Vic 3122, Australia*

[b]*University of Science and Technology, University of Da Nang, Vietnam*

[†]*E-mail:* kdinh@swin.edu.au

Received 28 May 2018

Accepted for publication 13 June 2018

Published 23 June 2018

Abstract. *Coherent diffractive imaging (CDI) is a lensless microscopy technique in which the structure of a specimen of interest is probed using a coherent short-wavelength light source. CDI has been widely used in nanotechnology and structural biology to capture high resolution images of non-crystalline objects. In this paper, we review the theoretical and experimental aspects of coherent diffractive imaging using a focused narrow-bandwidth table-top high harmonic source. The review begins with an outline of generation and characterization of the high harmonic source. Theoretical description of coherent diffractive imaging technique is then summarized. The review concludes with our recent results in imaging using a single harmonic beam selected by employing XUV focusing mirrors. These achievements provide a promising technique for the non-crystallographic structural determination of membrane proteins using a table-top extreme ultraviolet source.*

Keywords: laser applications, nonlinear optics, imaging reconstruction.

Classification numbers: 42.30.Wb, 42.62.-b, 42.65.-k.

I. INTRODUCTION

Visualization of the structure of nanoscale objects based on microscopy is crucial to study dynamic processes in material and biological systems [1]. Conventional microscopy allows a spatial resolution of 200 nm to be resolved. This resolution is typically limited to λ/2NA, where λ is the wavelength of the light source and NA is the numerical aperture. Scanning probe microscopy techniques such as atomic force microscopy or scanning force microscopy have been made impressive progress for super-resolution imaging with a resolution of the order of fractions of a nanometer [1]. However, they are limited to surface structures and are not able to allow us to make a morphological analysis. Electron microscopy which uses a particle beam of electrons to illuminate a crystalline structures and to produce a magnified image at the atomic level is well established as a powerful method for obtaining images with sub-optical wavelength resolution [2]. However, this technique is restricted to imaging thin samples and suffers from a relatively low image contrast in most cases. For samples with thickness more than 500 nm, because of inelastic scattering, this technique produces a blurred image and low resolution [3]. To investigate thick samples such as biological specimens, based on the innovation of imaging and labelling techniques, S. M. Hurtley and L. Helmuth developed a far-field light microscope which is able to image living cells with a resolution of about 200 nm [4]. Using extreme ultraviolet or soft x-ray radiation as a light source allows us to obtain high resolution imaging of thick samples [5]. A conventional lens with solid state material which has a strong absorption of soft x-rays cannot be used for XUV radiation focusing and therefore in x-ray microscopy diffractive optical elements such as Fresnel zone plate lenses with very short focal lengths are employed to produce high magnification. By using a condenser zone plate lens to illuminate the sample with x-ray radiation of 1.5 nm wavelength and a micro-zone plate lens to project an image onto a CCD camera, W. Chao *et al.* [6] achieved a spatial resolution down to 5 nm with a state-of-the-art zone plate. However, for x-ray microscopy, at very high magnification, zone plates have a relatively short working distance and a small depth of focus that leads to the potential for large chromatic aberration. Moreover, since the zone plates block much of the light, there is only around 10% efficiency in the first order diffracted light [5]. Another imaging method with extreme ultraviolet or soft x-ray radiation is holography, such as Fourier transform holography [7]. By using coherent x-ray radiation from a synchrotron, this approach has been used to image gold test objects with a resolution less than 60 nm. However, this method is limited by the need to surround the specimen with a large highly transmitting region.

Therefore, new techniques for high resolution imaging of thick samples which overcome the shortcomings of the previous methods are of great interest. Coherent diffractive imaging (CDI) using short wavelength light in the extreme ultraviolet or soft x-ray regions has emerged as a promising alternative approach to address the above problems [8–14]. CDI was first demonstrated in 1999 using the light from a synchrotron by J. Miao *et al*. [14]. Instead of using optical elements, in CDI the sample to be investigated is illuminated with a spatially coherent light source and the object is reconstructed from the diffraction pattern recorded on a CCD camera by means of iterative computer-based reconstruction algorithms [8–14]. When an object is exposed to light from a coherent source, a diffraction pattern of the object is captured and based on diffraction and propagation theory the complex electric field of the light diffraction can be considered as a Fourier transform of the object. The object's image is then reconstructed by performing an inverse

Fourier transform. Because only the intensity of the diffraction pattern is recorded a Fourier-based iterative phase-retrieval algorithm combined with an over-sampling method is used to recover the phase for image reconstruction process. This "lens-less" technique is aberration-free so that it is suitable for use at extreme UV and soft X-ray wavelengths and the theoretical spatial resolution is limited only by the radiation wavelength. In addition, because x-ray radiation can penetrate thicker samples, the CDI technique can overcome the limitations of an electron microscope and can be used as a promising approach for high resolution imaging of thick samples, especially for biological samples. Based on this technique, the structure, shape and size of finite non-periodic objects have been determined [15–20]. Using x-rays from a synchrotron, D. Shapiro et al. have examined a frozen dried yeast cell and its internal components with about 30 nm resolution [21]. Using a soft x-ray free electron laser, H. N. Chapman et al. have successfully imaged a nanostructured non-periodic object with a spatial resolution down to 60 nm [22]. Also, three dimensional reconstruction of objects has been performed successfully at 50 nm resolution [23]. C. G. Schroer et al. have shown that by focusing hard x-rays on a sample in the form of a small gold particle, a spatial resolution of about 5 nm can be obtained [20]. It is worth noting that coherent illumination of the object is crucial to this technique, and the coherent dose on the sample determines the spatial resolution.

Besides the radiation from synchrotrons [9] and free electron x-ray lasers [10], high harmonic generation (HHG) sources can be used for illumination in XUV and soft x-ray imaging, with their ultra-short pulses, excellent coherence properties and high degree of tunability [8, 11, 13]. HHG which occurs in the interaction between an intense laser pulse and an atomic or molecular medium [24–26] provides excellent coherence properties and high degree of tenability. In addition, compared to synchrotron and x-ray laser sources, a HHG source enables a small scale microscopy.

In this paper, we review theoretical background of coherent diffractive imaging technique. We also summarize those figures of high harmonic generation that are applicable to the development of CDI. Our recent achievements in CDI with a focused narrow bandwidth HHG source around 30 nm are then presented.

II. THEORETICAL BACKGROUND OF CDI

In coherent diffractive imaging technique, an object is illuminated by a coherent light source and the intensity of the diffraction pattern is recorded by a detector. The free space propagation of the complex wave field from the object plane $U(x_1,y_1)$,where $x$and y are horizontal and vertical co-ordinates to the detector plane, $U(x_0,y_0)$, is described by the far field approximation as [27,28]

$$U\left(x_0,\ y_0\right)=\frac{-e^{-\frac{2\pi iz}{\lambda}}}{i\lambda z}e^{-\frac{2\pi i\left(x_0^2+y_0^2\right)}{2\lambda z}}\ \times F\left\{U\left(x_1,y_1,z\right)\right\} \tag{1}$$

where $z$is the distance between the sample and the detector , λ is the wavelength of the incident beam and F denotes the Fourier transform operator.

The intensity of the diffraction pattern is given by the square modulus of $U(x_0,y_0)$. The sample image can be reconstructed from the intensity distribution of the diffraction pattern when the phase information is known. However, in experimental work, there is only the intensity of the diffraction field given by the modulus of squared $U_i(x,y,z)$ to be recorded and all the phase information is lost. Therefore, a Fourier-based iterative phase-retrieval algorithm is used to recover the phase for reconstruction of the image. Generally, an iterative phase retrieval algorithm consists

of the following four basic steps involving iterative Fourier transformation back and forth between the object and Fourier domains and application of the measured data or known constraints in each domain [29, 30].

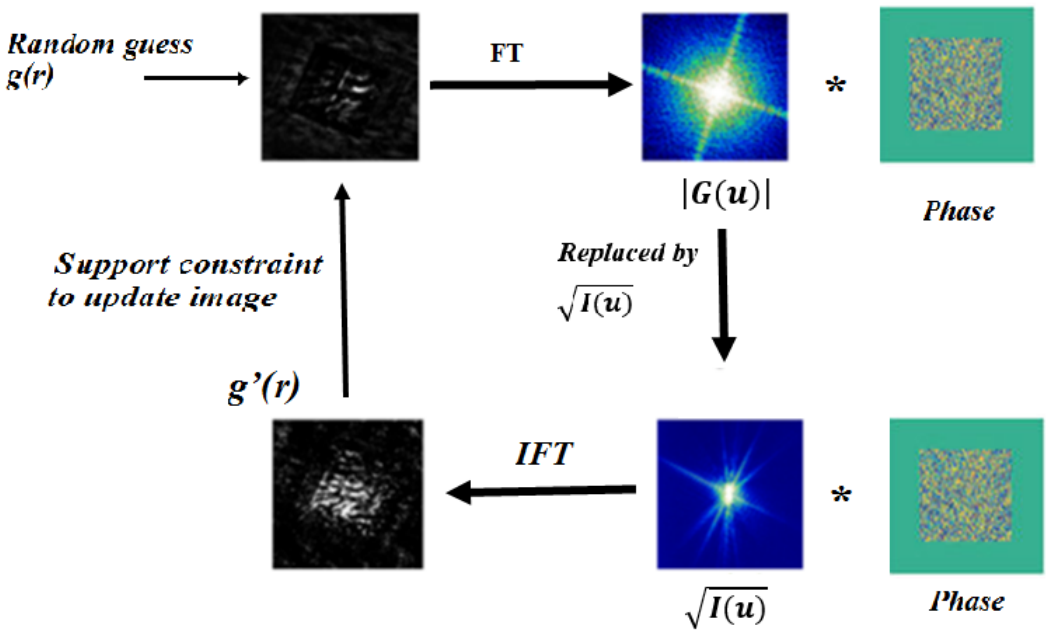

Fig. 1. The reconstruction process.

In the reconstruction process, as illustrated in Fig. 1, the sample's image is initialized with a random guess, or a support image, $g(r)$. The magnitude and phase at the detector plane described by $G(u)$ are then calculated by taking a Fourier transform of the initialized sample. After that, the magnitude of $G(u)$ is replaced by the Fourier modulus (square root of the diffraction intensity recorded by the detector, $\sqrt{I(u)}$), and the new sample's image in real space is calculated by taking an inverse Fourier transform of the updated $G(u)$.A support constraint is then applied to the image to obtain the updated sample's image, including the ER (Error Reduction) and HIO (Hybrid Input Output) algorithms. The ER algorithm is based on the assumption that the object is of finite size and is isolated in empty space, i.e., the ER operation sets all the intensities outside the support to zero while it keeps the intensities which are inside. Although ER helps to clean up the noise around the object, the operation may stagnate at a local minimum and prevent further convergence. On the other hand, the HIO operation takes into account feedback of the previous reconstructed image to the current image and allows non-zero amplitudes outside the support. This algorithm helps to escape the local minima. Therefore, combining HIO and ER is an effective method in the phase retrieval process.

In order to obtain a high-quality reconstructed image of the sample experimental parameters including the quality of the harmonic emission, the distance between the sample and the detector and the sample size need to meet the following requirements [30]. First, the illuminating beam

must be coherent and have a reasonably narrow bandwidth ($\lambda/\Delta\lambda > 100$). Secondly, the spatial coherence length of the source needs to be as large as the sample size times the linear oversampling factor. In addition, the harmonic photon flux density needs to be sufficiently high to capture diffractive patterns at high diffraction angles, but not too high as to damage the sample. The sample should be also placed far enough from the detector to ensure that a far-field diffraction pattern is recorded and the Fraunhofer criterion is satisfied. In this case, the theoretical resolution of the CDI method can be estimated from $\delta = 0.61\lambda/NA$, where *NA* is the effective "numerical aperture" of the scattered radiation.

When high harmonic generation source is utilized for CDI, due to its nature, the source consists of a beam of multiple longitudinal coherent modes whereas as stated above the image reconstruction process requires an entirely coherent wave field. Consequently, CDI is usually carried out with a single harmonic order of the harmonic spectrum which is selected by using a monochromator or a narrow band spectral filter. Besides monochromatic CDI, polychromatic CDI has been developed since it is necessary for the illuminating beam in the short-wavelength range ($<$ 10 nm), especially in the water window (4.4 to 2.3 nm,) where it is not possible to extract a single monochromatic component enabling the conventional CDI approach to be applied [31–33]. In addition, polychromatic CDI allows us to utilize as much of the emitted photon flux as possible in order to keep the acquisition time short and thus avoid possible long term instabilities of the harmonic source. In the past, our collaborators have demonstrated a reconstructed resolution of $\sim$ 100 nm for a periodic sample image from a 300 s integration-time diffraction pattern and a square sample size of $\sim$ 15 μm by employing HHG radiation from an argon source (wavelength $\sim$ 30 nm) with about 5 harmonic orders [31–33].

Recently, CDI using a single harmonic beam selected by employing XUV focusing mirrors has been implemented to achieve a significant advance in imaging resolution and data acquisition time [11, 13, 34, 35]. The focusing mirror allows the illuminating beam to be confined to a smaller area (¡ 50 μm) which is comparable to the size of the sample leading to an increase of the total photon flux illuminating the sample, i.e., a significant reduction in the acquisition time of a high-dynamic range diffraction pattern. Because of the use of a focusing mirror, the effect of the curvature field on the diffraction pattern and the reconstruction process needs to be considered, i.e., the variation of the phase and intensity of the illumination beam across the sample needs to be taken into account. Indeed, the curvature of the incident field can be corrected by considering a phase variation at the sample plane and therefore Eq.1 can be rewritten as

$$U(x_0,\, y_0) = \frac{-e^{-\frac{2\pi i z}{\lambda}}}{i\lambda z} e^{-\frac{2\pi i\left(x_0^2+y_0^2\right)}{2\lambda z}} \times F\left\{U(x_1, y_1, z)\exp\left(\frac{i\pi\left(x_1^2+y_1^2\right)}{\lambda d}\right)\right\} \tag{2}$$

where d is the distance from the focus position to the sample plane.

It is shown that there is a new phase term, $\exp\left(\frac{i\pi\left(x_1^2+y_1^2\right)}{\lambda d}\right)$, to be added to the Fourier transform operator. This phase term is applied to simulate the curvature of the field in the sample plane, which is analogous to a known "fitting parameter" for reconstruction. The phase retrieval algorithm is now modified by taking a Fourier transform of the product of the sample image and this new phase term. Adding this parameter results in a faster convergence of the reconstruction process, leading to reduction of the reconstruction time [36].

III. HIGH-ORDER HARMONIC GENERATION

High Harmonic Generation is an extreme nonlinear optical process in which the frequency of laser pulse is converted into its integer multiples. Harmonics of very high orders which are coherent radiation in the extreme ultraviolet (XUV) radiation and soft X-ray region are generated when an intense laser pulse is focused into a noble gas [24, 25]. A physical understanding of the generation of high-order harmonics can be explained using the semi-classical model, called "the simple-man theory" or three-step model in which the interaction between the laser field and the atoms is separated into ionization, acceleration and recombination stages [24, 25]. A full quantum mechanical theory which considers quantum effects such as tunneling, diffusion and interference has been developed within the strong field approximation (SFA) model to describe aspects of the HHG process more precisely [37]. In the SFA theory, the HHG from a single atom can be obtained by calculating the dipole acceleration of a returning electron which has gained momentum in the presence of the oscillating laser electric field. However, the single atom response theory does not completely describe the experimental harmonic-generation process in a medium. In order to achieve good agreement between theory and experiment, one must also take into account the effects of propagation and phase mismatch between the harmonic field and the fundamental field in the macroscopic medium [38, 39].

Assuming that the Rayleigh length is much longer than the interaction length, i.e., over the interaction medium the fundamental laser beam profile is almost unchanged and the generating conditions can be considered to be homogeneous over the whole the medium, the number of photons emitted on-axis per unit of time and area is given by [40]

$$N_{out} \propto \rho^2 d_q^2 \frac{4L_{abs}^2}{1+4\pi^2(L_{abs}^2/L_{q,coh}^2)} \left[1+\exp\left(-\frac{L_{med}}{L_{abs}}\right)-2\cos\left(\frac{\pi L_{med}}{L_{q,coh}}\right)\exp\left(-\frac{L_{med}}{L_{abs}}\right)\right] \quad (3)$$

where ρ is the gas density, d_q is the recombination dipole of the q^{th} harmonic, L_{med} is the interaction length, L_{abs} is the absorption length, and $L_{q,coh}$ is the coherence length of the q^{th} harmonic which can be expressed as a function of the phase mismatch Δk_q

$$L_{q.coh} = \frac{\pi}{\Delta k_q} \quad (4)$$

The phase mismatch Δk_q is the sum of four terms which can be expressed as [41, 42]

$$\begin{array}{c} \Delta k_q = \frac{2\pi q}{\lambda} p\delta n(1-\eta) - \eta p N_{atm} r_e \lambda (q-\frac{1}{q}) \\ +(geometric\,term)+(atomic\,phase) \end{array} \quad (5)$$

where λ is the laser wavelength; p and η are the gas pressure and ionization fraction, respectively; $\delta n = n_{laser} - n_q$; n_{laser} and n_q are the refractive indices for the fundamental and the q^{th} harmonic field; N_{atm} is the atomic number density at 1 atm; and r_e is the classical electron radius.

In Eq. (5) the first (positive) term is related to the medium dispersion and the second (negative) term is due to the plasma dispersion. The geometric term is negative in a waveguide [43] or self-guide [44]. For a focused Gaussian beam the geometrical phase shift around the focal point is due to the Gouy phase shift. To a first approximation the atomic dipole phase scales linearly with the laser intensity. For phase matching in the HHG process, one needs $\Delta k_q = qk_0 - k_q = 0$, where k_q is the wavevector of the q^{th} harmonic and k_0 is the wavevector of the fundamental beam. In this case, there is a coherent construction of the harmonic emission. In addition, the transfer

of coherence properties between the driving laser and harmonic radiation is most effective to obtain highly coherent XUV radiation. Proper adjustment of the macroscopic parameters such as the effective interaction length, the laser intensity and the gas pressure can be used to modify the HHG spectrum because the variation of the macroscopic parameters influences the atomic density and the ionization fraction, and the macroscopic phase matching that can be achieved. When varying these parameters not only the number of harmonic orders but also the spectral weighting within that particular spectral range changes. Consequently, for different experimental conditions, the harmonic generation can be phase-matched and confined to just a few harmonic orders in a particular range of spectrum.

IV. EXPERIMENT

IV.1. Experimental setup

The high order harmonics are emitted by a laser system consisting of a 1 kHz multi-pass chirped-pulse amplifier (Quantronix Odin-II HE) that is seeded by a Ti:Sapphire oscillator. This laser system generates 30 fs pulses centred at 805 nm and the unapertured and unfocused beam has an average diameter of 12 mm and an energy of 2 mJ.

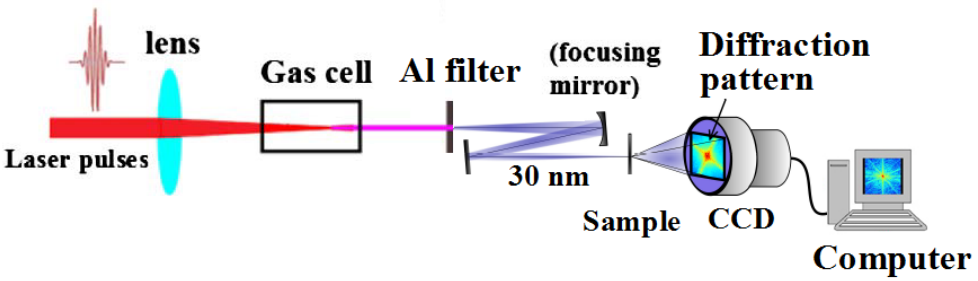

Fig. 2. Experimental setup.

The driving laser beam is focused into a 150 mm-long argon gas cell by a 300 mm focusing lens which is mounted on a precision x/y/z translation stage to allow proper alignment with respect to the centre of the laser beam and to move the laser focus longitudinally with respect to the exit plane of the gas cell. A stabilization system, which consists of a single valve pressure regulator (Alicat), a ceramic capacitance pressure gauge (Pfeiffer CMR 361), a TPG 256A MaxiGauge controller and a LabView program on a computer is used to control the pressure inside the gas cell. The gas cell has a glass window for entry of the laser pulses and a 0.1 mm pinhole at the exit to isolate the vacuum chamber from the argon gas-filled cell and to out-couple the harmonic emission. An ultra-thin aluminium filter which has high transmission in the wavelength range of 17–60 nm and is mounted on a filter wheel controlled by an electric motor is used to remove the fundamental beam. After that, a spatial set consisting of several pinholes with a dimeter ¡ 2 mm and placed precisely along the beam path is used to provide precise spatial filtering for the illuminating signal. The harmonic beam is then focused into the sample by a pair of mirrors comprising a plane mirror (M1) and a 20 cm-radius focusing mirror (M2) (commercial Optix Fab multilayer Mo/Si

mirrors with 2 nm bandwidth and 35% reflectivity at 30 nm (for each mirror) which are installed at a reflection angle of $\sim 10^0$ in a Z-configuration to reduce astigmatism of the focusing. The sample to be investigated is mounted on a sample holder which allows precision alignment of the sample in the three directions x, y and z using an x-y-z motorized translation stages. The diffracted emission of the sample after illumination with the focused harmonic beam is detected by a deep-cooled 16-bit resolution CCD camera (Princeton Instruments PIXIS 2048×2048) with 13.5×13.5 μm pixel size. The camera is placed 3.5 cm behind the sample and is cooled to -40˚C to minimize thermal noise when taking diffraction data. The whole CDI apparatus downstream from the gas cell is placed inside the vacuum chamber which is pumped by a turbo molecular drag pump (Pfeiffer Vacuum TMU 262) at a pressure $\sim 10^{-5}$ Torr.

Traditionally, the image reconstruction program runs on a single CPU computer. This process requires a long time to complete since it deals with a large amount of data and several thousand of computation iterations. In order to reduce the consumption time of the reconstruction process significantly, we implement the reconstruction algorithm on a graphical processing unit (GPU) in which a Tesla K20c GPU is installed. The calculation is spread over a massive number of parallel computational units. Featuring 2496 computational units (CUDA cores), the GPU is capable of processing 1.17×10^{12} double-precision floating-point operations per second (flops), which is about 10 times better than a typical Intel Core i7 CPU.

IV.2. Preparation of samples

In our work, two kinds of samples are investigated, transmission samples and absorption samples. First, the two "SWIN" samples, (3 μm $\times$ 3 μm) and (7 μm $\times$ 7 μm) are demonstrated. The samples are fabricated on a 50 nm thick Si_3N_4 membranes and both sides are coated with 50 nm and 150 nm-thick gold layers to ensure that the membranes are almost opaque to the illuminating beam. The SWIN pattern is milled using ion beam lithography. Their scanning electron microscopy (SEM) images are shown in Fig. 5(a) and Fig. 6(a). Because of milling on the gold-coated Si_3N_4 membranes the wave field is 100% transmitted through the letter patterns while the background is completely "dark". In addition, the sample thickness is much smaller than its size. Therefore, these samples can be considered as transmissive binary samples and the exit surface wave is the same as the sample's image.

However, in practice transmission samples, such as the SWIN samples, are not scientifically similar to real-biological specimens. Because the x-ray radiation is strongly absorbed by most materials, the reconstructed images of the real biological samples will be inverted, i.e., the object of interest will be displayed as dark on a bright background. Hence, we also conduct the CDI experiments with two absorption samples, whose characteristics are similar to the real biological samples. The first sample (sample A) was fabricated simply by evaporation of a $\sim$0.2 μL of an aqueous, dilute solution of monodisperse 2 μm silica (10% wt solid) particles (Polyscience Inc (USA)) mixed with some 400 nm Amino Polystyrene nano-particles (Invitrogen, 2% (W/v)), which are dispersed by sonication for 30 minutes prior to preparation, on a 30 nm thick Si_3N_4substrate (Norcada Inc.). The 2 μm silica particles cover $\sim$ 75% of the window area and only few 400 nm particles can be seen in the scanning electron microscopy images shown in Fig. 7(a). The second sample (sample B) was fabricated by evaporating a solution of2 μm-Carboxylated Polystyrene and a few 400 nm-Amino Polystyrene nano-particles on a 30 nm thick S_{i3N4} membrane. The density of particles is low so the reduction in the transmission is less than 30% as

shown in Fig. 8(a). The Si_3N_4 membrane has a rather high transmission ($\sim$ 40%) at the 30 nm illuminating wavelength, and presents as a "window" of $\sim$13$\times$13 μm in a larger opaque solid substrate. This window acts as the support boundary in the CDI reconstructions. Both the silica and polystyrene particles used in the samples are opaque to the 30 nm harmonic beam. For these two samples, all particles doped are opaque to this wavelength and therefore they can be considered to be constructed from absorption functions. This characteristic is very similar when imaging biological samples, in which the contrast of the image is resulted from the difference of the atoms' absorption edges between the sample and the membrane or between different materials in the sample itself.

IV.3. Generation and characterization of the illumination source

Since the maximum reflectivity of our XUV focusing mirror is at 30 nm we aim to obtain a few harmonics source around 30 nm. The typically required spectrum which is captured by inserting a spectrometer into the harmonic beam path and shown in Fig. 3(a) is generated when the argon pressure of the cell is measure to be 60 Torr, the laser energy is around 1.2 mJ corresponding to a laser intensity of 2×10^{14} W/cm^2 and the focus position is approximately 2 mm inside the gas cell [45]. By using narrow bandwidth reflective and focusing mirrors, a single harmonic at around 30 nm (27^{th} harmonic) is isolated and focused into the sample while the contributions of the two neighbouring harmonics can be negligible, leading to a small bandwidth source ($\lambda/\Delta\lambda > 250$). Consequently, the illumination field can be considered as a monochromatic source for the image reconstruction process.

As mentioned in section II, in order to successfully reconstruct the image of the sample, the spatial coherence length of the illuminating source must be about as large as the sample size times the linear oversampling factor. Thus, before conducting the CDI experiments, a Young's double slit experiment is performed using a Young's double slit consisting of two parallel 4 μm $\times$ 100 μm slits, with a spacing of 20 μm in order to determine the degree of spatial coherence of the HHG source. The experimental setup for this measurement is similar to that used for the CDI experiment where the pair of mirrors (M1 and M2) and the CDI samples are not installed and the spectrometer is attached. The Young's double slit is etched into a silicon wafer which is mounted on a slit holder and placed at $\sim$ 60 cm from the CCD. By inserting a spectrometer into the beam path and mounting the YDS perpendicular to the slit of the spectrometer, the interference fringes of each harmonic observed along the X-direction of the CCD are directly recorded in the Y-direction. Based on the interference pattern shown in Fig. 3(c), the degree of spatial coherence of the harmonic source generated from argon for both cases (without the focusing mirror and with the focusing mirror) is $\sim$ 0.99 [45]. This indicates a very high spatial coherence of the HHG source.

One of the important parameters we need to know before conducting the CDI experiment is the illuminating beam profile around the focus point. This parameter helps us to determine the position of the sample and the effect of the curvature of the field. In order to perform this task, a diffraction scanning experiment with two 5 $\times$200 μm slits in an X-Y configuration is carried out. The intensity profile of the beam is measured directly from the diffractive intensity which is recorded in the CCD camera during the scanning of the slit across the beam. Fig. 3(d) shows the beam profile of the HHG beam along the x-axis around the focus point ($\pm$ 2.5 mm). It is clear the FWHM beam size is measured to be 7 μm, 15 and 25 μm at the focus and at the distances

$\sim$ 1.5 mm and $\sim$ 2.5 mm, respectively. A similar result is observed when scanning the slit ($\pm$2.5 mm around the focus point) along the y-axis. This confirms a good focusing geometry in our experiments.

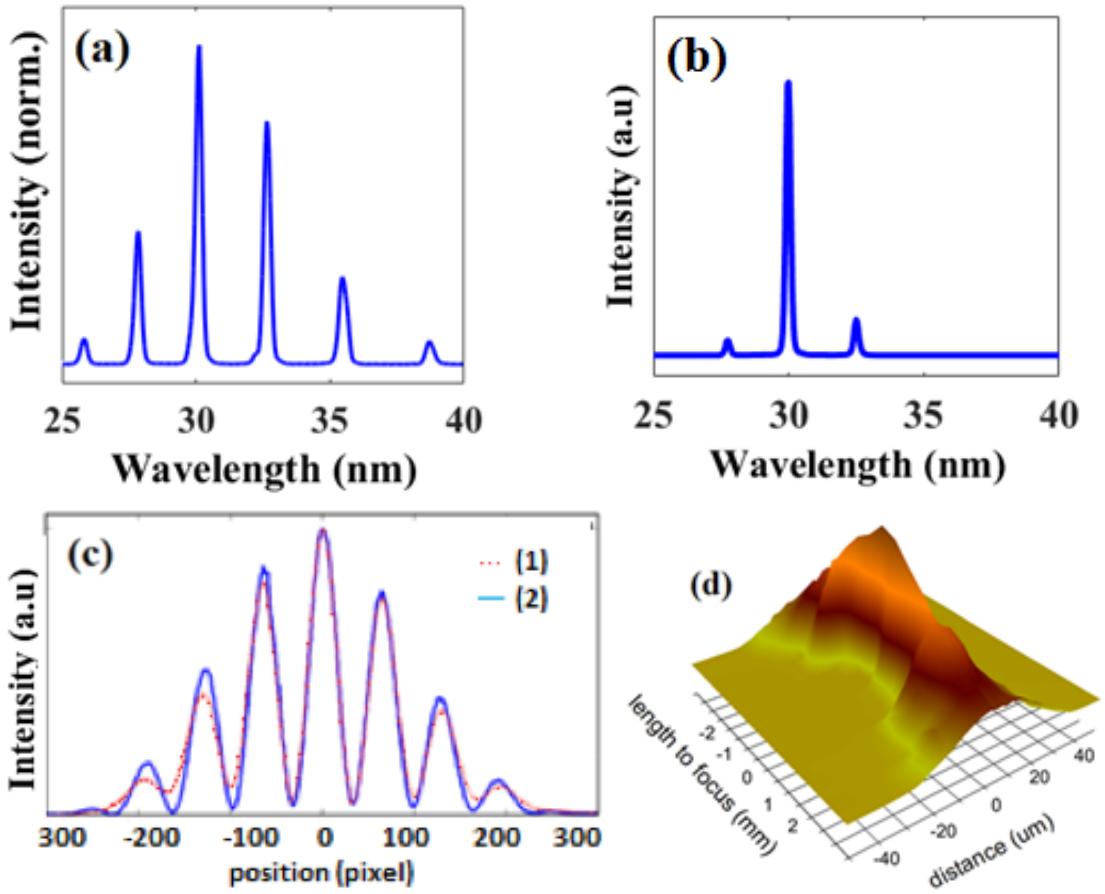

Fig. 3. The HHG spectrum without the focusing mirror (a) and with the focusing mirror (b). The interference fringes obtained without the focusing mirror (1) and with the focusing mirror (2) (c). The measured illuminating beam profile (d).

IV.4. Measuring the spectrum of the illuminating source

In order to successfully reconstruct the object's image, a highly coherent spectrum of the source needs to be acquired under the same experimental conditions with the collection of the diffraction image. However, it is impossible to perform this task by using a spectrometer since it could not been installed when the diffraction pattern is taken. Therefore, a new technique is applied to address this challenge, in which the source's spectrum is determined by analysing the diffraction pattern of a predefined sample. In this experiment, a sample consisting of a 6 μm $\times$ 6 μm array of pinholes, which are milled on a Si_3N_4membrane and shown in Fig. 4(a), is used to determine the source's spectrum from its diffraction pattern. Each pinhole is 180 nm wide in diameter and

the distance between two centres is 280 nm. The sample allows the diffraction pattern to be only observed at the reciprocal lattice points. When there is no focusing mirror, i.e., the source consists of multiple harmonics, the diffraction pattern is an incoherent superposition of the diffraction by each harmonic incident on the sample‘ [46]. Fig. 4(b) and Fig. 4(c) show the diffraction patterns of the sample using the HHG beam without and with the focusing mirror, respectively. In Fig. 4(d) and Fig. 4(e), the horizontal cross sections of selected areas marked with the rectangles show the relative contribution of different wavelengths to the illumination process [45]. These plots are in good agreement with the measured spectra which are seen in Fig. 3(a) and Fig. 3(b).

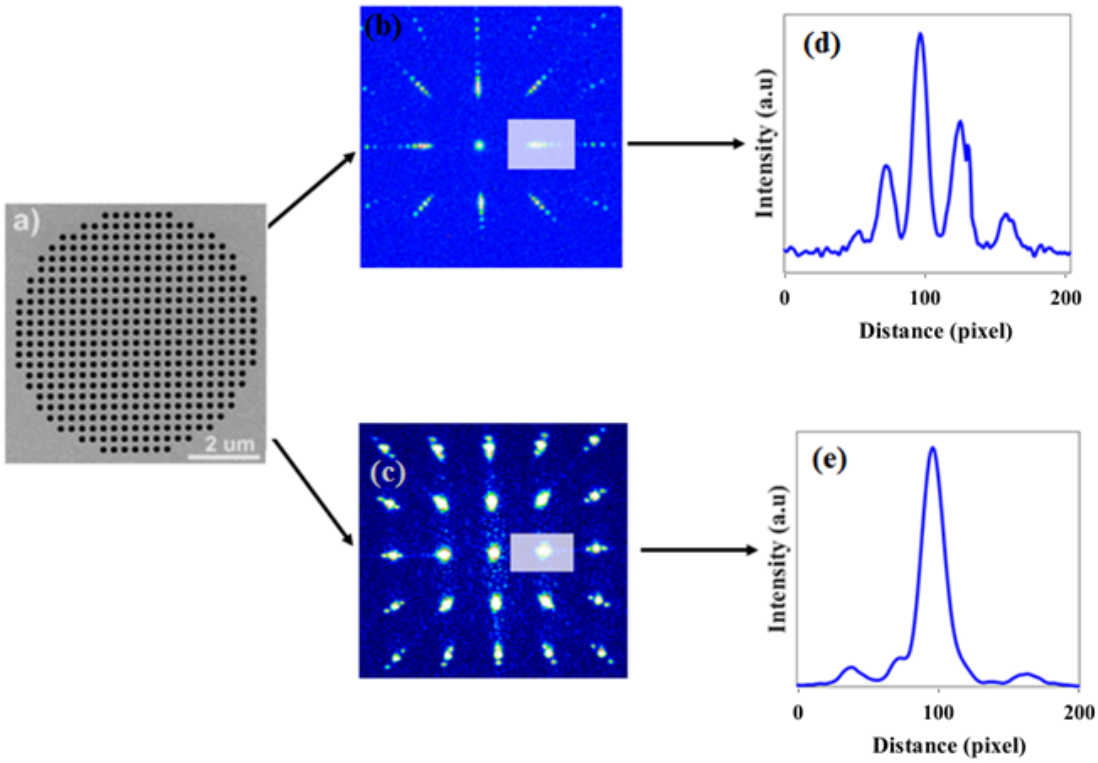

Fig. 4. Scanning electron microscope image of a sample consisting of an array of pinholes (a). Measured diffraction patterns using the HHG source without the XUV mirror (b) and with the XUV mirrors (c). Cross sections of the marked areas of the diffraction patterns without the mirror (d) and with the mirror (e).

IV.5. Coherent diffractive imaging with transmission sample

Two “SWIN” samples which are considered as transmission samples are used for the study. For each of the SWIN samples, diffraction patterns are taken at various distances, $\pm$ 2.5 mm and $\pm$ 1.5 mm, relative to the focus point, where positive distances mean behind the focus point. The different size of the samples, i.e., (3 μm $\times$ 3 μm) and (7 μm $\times$ 7 μm), allows us to investigate the influence of the curvature of the incident wave field on the reconstruction when the focused HHG beam’s size is comparable to the sample’s size.

By controlling various experimental parameters, such as gas pressure, fundamental laser energy and the position of the laser focus, the high harmonic generation process is optimized with strongest intensity around 30 nm. The band-pass mirror allows one strong narrow bandwidth harmonic at a wavelength around 30 nm (H27) to be selected to illuminate the sample. Small contributions from the 25th and 29th harmonic orders are not reflected in the diffraction image. The sample is then positioned at the appropriate transverse and longitudinal coordinates so that the centre of the diffraction pattern coincides with the centre of the CCD which is cooled down to -40 ˚ C equilibrate thermally.

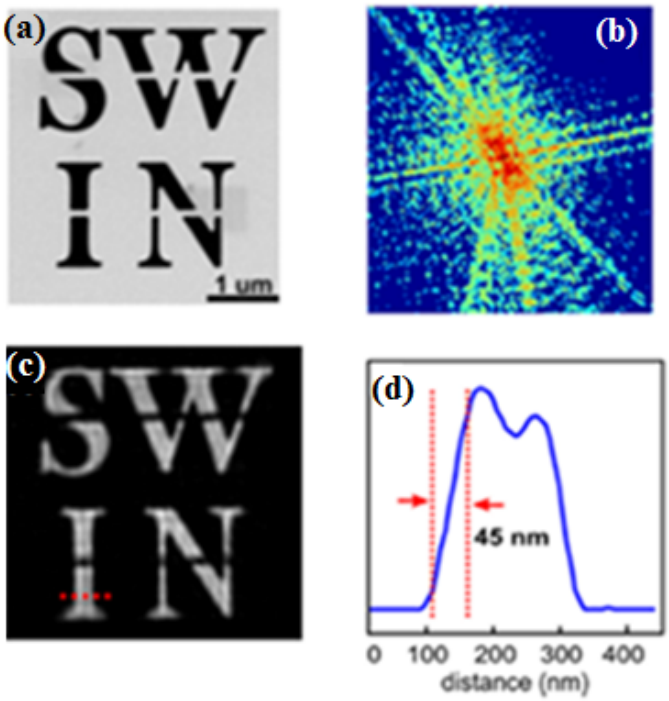

Fig. 5. Small SWIN sample: Scanning electron microscope image (a). Diffraction image at the distances 2.5 mm (b). The reconstructed image (c). A cross section of the letter "I" from the reconstructed image (d).

At a distance of $\pm$ 2.5 mm, it takes 8 s to capture a full dynamic range ($\sim$65000 counts) diffraction image of the small SWIN sample, while the large SWIN sample requires 2 s. When the samples are placed closer to the focus point, i.e., at $\pm$ 1.5 mm, the effective photon flux is significantly increased; hence the required exposure times are only 4 s and 1 s for the small and large SWIN samples, respectively. In order to obtain a good diffraction image for reconstruction process, 20 diffraction patterns and another 20 background images are taken for each sample and averaged to increase the signal to noise (S/N) ratio. The background image is taken when the gas cell is completely vented, i.e., when no harmonic can be generated. The final diffraction pattern is obtained after subtraction of the averaged background from the averaged diffraction pattern, where negative intensity is rounded to zero. The Error Reduction (ER) and Hybrid Input Output (HIO)

algorithms are used for reconstruction process. A rectangle whose dimension is sufficiently larger than the sample size is used as a support constraint. The size of this rectangle which has a minor influence on the resolution of the reconstructed image can be determined from the first few HIO iterations.

For the small SWIN sample, at a distance of $\pm$ 2.5 mm, the focused beam's diameter is eight times larger than the sample size, leading to an intensity variation of the illuminating field over the sample of less than 5% and therefore the condition for a uniform illuminating field is satisfied. The diffraction images and the reconstructed images of this sample are shown in Fig. 5(b) and Fig. 5(c), respectively. To determine the resolution of the reconstructed images, a knife-edge test is performed [47]. A cross section of the leg of the letter I from the reconstructed images (Fig. 5(d)) reveals a spatial resolution of $\sim$45 nm (10%–90% of intensity profile). This value is in good agreement with the theoretical estimate ($\sim$ 47 nm) based on the Rayleigh criterion.

When this sample is placed at a distance of 1.5 mm from the focus point, the diameter of the illuminating beam is still four times larger than the sample size and the plane-wave field approximation is still valid for the reconstruction. Thus, a similar recovered image to that shown in Fig. 5(c) is still observed.

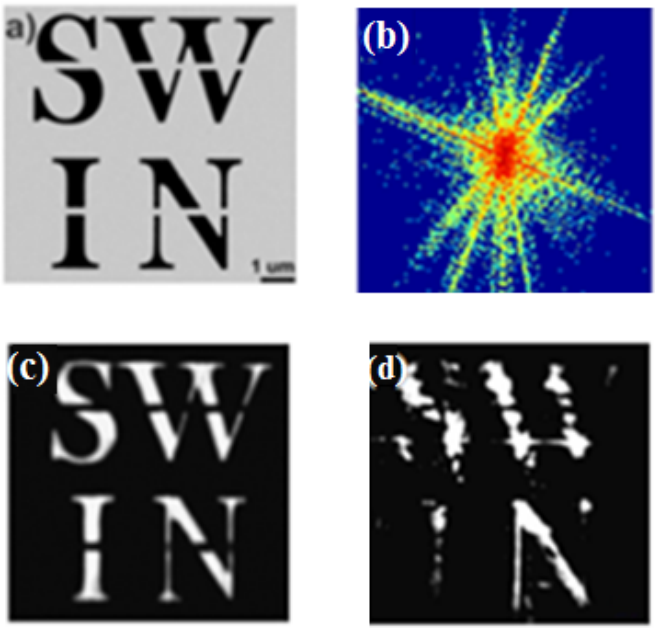

Fig. 6. Large SWIN sample: Scanning electron microscope image (a). Diffraction image at the distances 2.5 mm (b). The reconstructed image (c). The blurred reconstructed image (d).

For the large SWIN sample, at a distance of $\pm$2.5 mm, the focused beam's diameter is about 4 times larger than the sample size. Consequently, the uniform illumination can be applied. By using a plane wave approximation for the reconstruction, we are able to obtain a good recovered image with a spatial resolution of 60 nm. Fig. 6(b) and Fig. 6(c) show the diffraction pattern

and the reconstructed image of the large SWIN sample at this distance. However, at a distance of 1.5 mm, the beam size is only about two times larger than this sample's size. As a result, the curvature of the field needs to be considered. Due to the strong curvature of the field at the sample plane, the plane-wave approximation is no longer valid leading to a blurred reconstructed image, as shown in Fig. 6(d). When the curvature correction mentioned in section II is applied, the similar reconstructed image shown in Fig. 6(c) is produced. In other words, by placing the sample at a reasonable closer distance to the focus point and taking account the curvature correction, a good reconstructed image can be still achieved with a shorter exposure time.

If we move the sample closer to the focus (≤ 1.2 mm), it is difficult to resolve the sample's details since only part of the sample is illuminated by the harmonic beam and the diffraction is extremely distorted.

IV.6. Coherent diffractive imaging with absorption sample

In this study, sample A and sample B described in section IV.2 are used for imaging. This work can be performed without any adjustments to the experimental setup. These samples are completely different from the (binary) samples used in our previous experiments and by other groups since they are not only constructed from an absorption function and but also aperiodic. In addition, complex absorption coefficient of the spherical particles is smoothly decreasing. Such samples are very similar to real biological samples.

Two samples are placed at a distance ~ 3.5 mm beyond the focus point of the XUV focusing mirror. The exposure time is determined so that there is no pixel in the CCD to be saturated. With an exposure time of 30 s for the sample A and 3 s for the sample B diffraction images patterns with a rather high signal-to-noise (S/N) are captured within the maximum dynamic range of our CCD ($\sim 65,000$ counts).

For sample A, since the 2 μm silica particles which is opaque to the incident beam cover $\sim$ 75% of the window area, high-angle diffraction features can be clearly seen within the 512×512 array of the CCD without any saturation (Fig. 7(b)) and that is good enough for reconstruction. In other words, this sample could result in a high contrast in the reconstruction process. Fig. 7(c) describes its reconstructed image and Fig. 7(d) plots a cross section of one hole (marked with the red line) to reveal a spatial reconstruction of 250 nm [48]. However, since the complex absorption coefficient of the spherical particles which is smoothly decreasing and different from binary samples was not included in the reconstruction process, the reconstructed spatial resolution obtained by the knife-edge test is larger than the theoretical resolution ($\sim$ 192 nm).

For sample B, since the density of the particles which is opaque to the 30 nm harmonic beam is low, the transmission of the incident beam is high. Therefore, with the exposure time of 3 s, the diffraction signals without any saturated pixels only appear around the center part of the CCD area (Fig. 8(b)) and there is no high angle diffractive feature which can provide high resolution information to be captured. Consequently, its respective reconstructed image shown in Fig. 8(c) is very blurred. The high intensity "crosses" in the diffraction pattern originates from the square shape of the silicon nitride membrane window, which can then be resolved clearly in the reconstructed image.

IV.7. Enhancement of the resolution using a beam stop

In order to improve the resolution of the reconstructed image, high-angle scattering must be obtained. However, sample B has a very large transmission area, which quickly leads to saturation

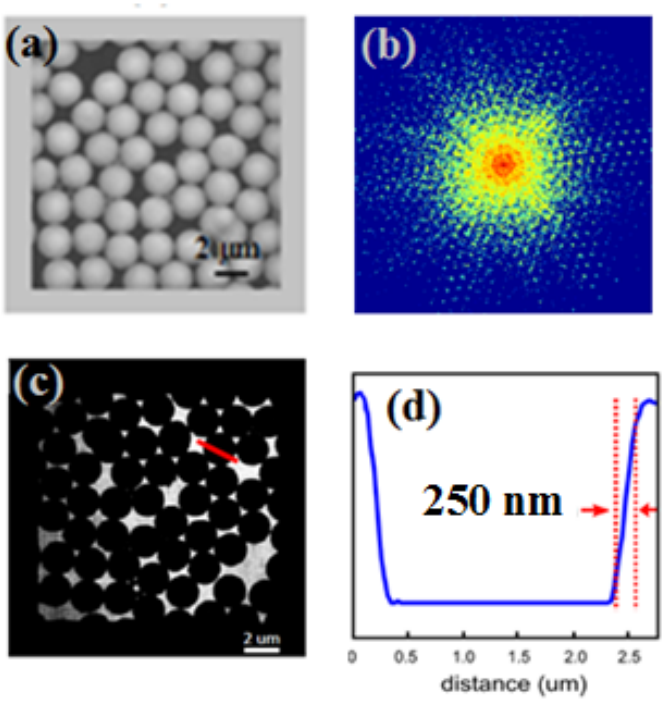

Fig. 7. Sample A: Scanning electron microscope image (a). Diffraction pattern (b). Reconstructed image (c). A cross section of one hole marked with the red line from the reconstructed image (d).

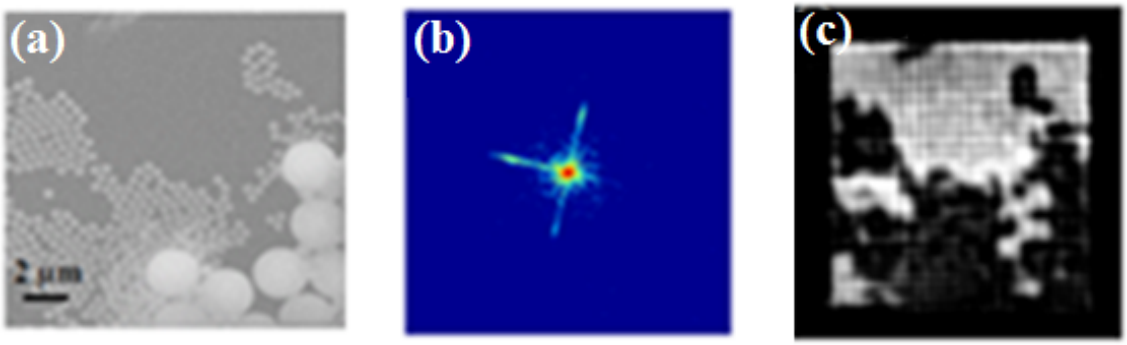

Fig. 8. Sample B: Scanning electron microscope image (a). Diffraction pattern (b). Reconstructed image (c).

of the detector. Thus, a design involving a metal beam stop and image stitching as well as a modified phase retrieval algorithm to process the new kind of data are employed to obtain high dynamic range diffraction patterns. The hand-made beam stop is of circular shape with a diameter 1.5 mm and is attached to micrometer-screws in the vertical direction of the flange by a very thin

brass wire (Fig. 9(a)) [49]. The beam stop is placed at a distance of 5 mm from the sensor of the CCD to minimize scattering of photons and reduce the shadow of the beam stop on the sensor. The beam stop is then adjusted to block intense speckles at the centre of the diffraction image. It can also be retracted to allow an undistorted diffraction pattern to be captured.

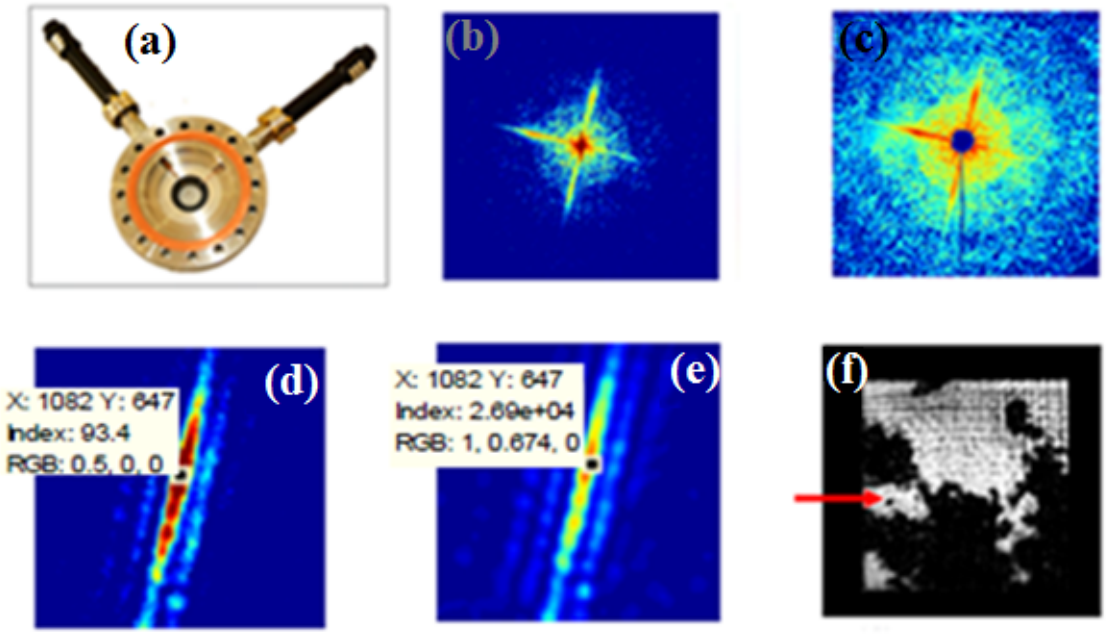

Fig. 9. Beam stop (a). Diffraction image of sample B without a beam stop for an exposure time of 40 seconds (b). Diffraction image of sample B with a beam stop for an exposure time of 5 minutes (c). Cropped diffraction pattern of sample B without a beam stop (d) and that with a beam stop (e). Reconstructed image of sample B with a beam stop and the red arrow indicating the single 400 nm particle (f).

The diffraction images are now in turn taken with a short exposure time without any saturation ($\sim$ 3 seconds), with longer exposure time with a saturated region (40 seconds) and with a very long exposure time with the beam stop until the highest intensity nearly reaches the maximum value ($\sim$ 65000) ($\sim$ 5 minutes). The latter two diffraction images are displayed in Fig. 9(b) and Fig. 9(c), respectively. The increase of the dynamic range can be estimated from the ratio of arbitrary intensity peaks at the same coordinate in the diffraction patterns without and with the beam stop. Fig. 9(d) and Fig. 9(e) show a comparison between the intensities of the chosen pattern for two cases and this ratio can be found around 288. This means that if the centre peak of the diffraction pattern taken without any saturation is replaced by the centre part of the diffraction pattern with the beam stop the new peak intensity will become $65000 \times 288 = 1.9 \times 10^7$, i.e., the dynamic range is enhanced to seven orders of magnitude. Regarding the reconstruction process when using beam stop, a modified reconstruction algorithm is applied as follows. First, a low resolution image of the sample as seen in Fig. 8(c) is recovered by using the diffraction pattern shown in Fig. 8(b). In the following, the center part of this diffraction image is stitched to the diffraction image taken

with 40 seconds. The low reconstruction image is now used as an initial guess for a new reconstructed image. The final diffraction image is then produced by combining the diffraction image obtained above and the diffraction image captured with the beam stop. The final reconstruction is performed using the final diffraction image and the reconstructed image acquired in the previous step is used as an initial guess for this reconstruction. The iteration number of the reconstruction process is about 1500 to 2000. During the reconstruction process, a rectangle whose dimension is larger than the sample size is used as a support constraint. The size of this rectangle can be determined from a first few HIO iterations. This size is flexible and only has a minor influence on the resolution of the reconstructed image. It is worth noting that for the imaging stitching process, the scaling factor can be estimated by performing scan trials of reconstruction so that the best quality image is shown.

Comparing Fig. 9(f) and Fig. 8(c), it is clear that finer details can be observed in the reconstructed image with the use of the beam stop. Especially, in Fig. 9(f) the single 400 nm particle indicated by the red arrow is clearly visible. This implies that the spatial resolution of the reconstructed image in the presence of the beam stop must be better than 400 nm [49]. Since other Amino Polystyrene particles form as a solid cluster, the individual particles are not distinguishable. However, these clusters in Fig. 9(f) are seen much more clearly than those in Fig. 8(c).

V. CONCLUSION

The emerging experimental and theoretical tools of coherent diffractive imaging using a focused narrow-bandwidth high harmonic generation source with a wavelength around 30 nm have been discussed. This technique is highly promising for imaging sub-10 nm objects using a shorter wavelength source and opens up the possibility of nanoscale-resolution imaging real biological samples using an inexpensive table-top soft x-ray light source.

REFERENCES

[1] F. J. Giessibl, *Rev. Mod. Phys*. **75** (2003) 949
[2] J. C. H. Spence, "High resolution electron microscopy," Oxford University Press, 3^{rd} edition (2009)
[3] C. Jacobsen, *Trends in Cell Biology* **9** (1999) 44
[4] S. M. Hurtley, and L. Helmuth, *Science* **300** (2003) 75
[5] D. Attwood, "Soft x-rays and extreme ultraviolet radiation," *Cambridge University Press*, 1^{st} edition (1999).
[6] W. Chao, B. D. Harteneck, J. A. Liddle, E. H. Anderson, and D. T. Attwood, *Nature* **435** (2005) 1210
[7] I. McNulty, J. Kirz, C. Jacobsen, E. H. Anderson, M. R. Howells, and D. P. Kern, *Science* **256** (1992) 1009
[8] R. L. Sandberg et al. *Phys. Rev. Lett.* **99** (2007) 098103
[9] D. Shapiro et al. *Proc. Natl. Acad. Sci. USA* **102** (2005) 15343
[10] H. N. Chapman *et al.*, *Nat. Phys.* (2006) 839
[11] A. Ravasio et al. *Phys. Rev. Lett.* **103** (2009) 028104
[12] H. N. Chapman and K. Nugent, *Nat. Photon.* **4** (2010) 833
[13] M. D. Seaberg et al. *Opt. Exp.* **19** (2011) 22470
[14] J. Miao, P. Charalambous, J. Kirz, and D. Sayre, *Nature* 400 (1999) 342
[15] I. K. Robinson, I. A. Vartanyants, G. J. Williams, M. A. Pfeifer, and J. A. Pitney, *Phys. Rev. Lett.* **87** (2001) 195505
[16] M. A. Pfeifer, G. J. Williams, I. A. Vartanyants, R. Harder, and I. K. Robinson, *Nature* **442** (2006) 63
[17] G. J. Williams, H. M. Quiney, B. B. Dhal, C. Q. Tran, K. A. Nugent, A. G. Peele, D. Paterson, and M. D. de Jonge, *Phys. Rev. Lett.* **9** (2006) 025506
[18] S. Marchesini, H. He, H. N. Chapman, S. P. Hau-Riege, A. Noy, M. R. Howells, U. Weierstall, and J. C. H. Spence, *Phys. Rev B* **68** (2003) 140101

[19] J. Miao, T. Ishikawa, B. Johnson, E. H. Anderson, B. Lai, and K. O. Hodgson, *Phys. Rev. Lett.* **89** (2002) 088303
[20] C. G. Schroer, P. Boye, J. M. Feldkamp, J. Patommel, A. Schropp, A. Schwab, S. Stephan, M. Burghammer, S. Schöder, and C. Riekel, *Phys. Rev. Lett.* **101** (2008) 090801
[21] D. Shapiro et al. *Proc. Natl. Acad. Sci. USA* **102** (2005) 15343
[22] H. N. Chapman *et al. Nat. Phys.* **2** (2006) 839
[23] H. N. Chapman et al. *J. Opt. Soc. A* **23** (2006) 1179
[24] J. J. Macklin, J. D. Kmetec, and C. L. Gordon, III, *Phys. Rev. Lett.* **70** (1993) 766
[25] P. B. Corkum, *Phys. Rev. Lett.* **71** (1993) 1994
[26] R. A. Bartels et al. Science 297 (2002) 376
[27] D. Sayre, Springer lecture notes in physics (M. Schlenker, Ed.) **112** (1980) 229 (Springer, New York).
[28] J. Miao and D. Sayre, *Acta Cryst. A* **56** (2000) 596
[29] J. R. Fienup, *Appl. Opt.* **21** (1982) 2758
[30] J. Miao, T. Ishikawa, E. H. Anderson, and K. O. Hodgson, *Phys. Rev. B* **67** (2003) 174104
[31] R. A. Dilanian, B. Chen, G. J. Williams, H. M. Quiney, K. A. Nugent, S. Teichmann, P. Hannaford, L. V. Dao, and A. G. Peele, *J. Appl. Phys*. **106** (2009) 023110
[32] B. Chen, R. A. Dilanian, S. Teichmann, B. Abbey, A. G. Peele, G. J. Williams, P. Hannaford, L. V. Dao, H. M. Quiney, and K. A. Nugent, *Phys. Rev. A* **79** (2009) 023809
[33] S. Teichmann, B. Chen, R. A. Dilanian, P. Hannaford, and L. V. Dao, *J. Appl. Phys.* **108** (2010) 023106
[34] H. V. Le, K. B. Dinh, P. Hannaford and L. V. Dao, *J. of Appl. Phys.* **116** (2014) 173104
[35] M. Zürch et al. *Sci. Rep.* **4** (2014) 7356
[36] H. M. Quiney et al. *Opt. Lett.* **30** (2005) 1638
[37] M. Lewenstein, P. Balcou, M. Y. Ivanov, A. L'Huillier, and P. B. Corkum, *Phys. Rev. A* **49** (1994) 2117
[38] A. L'Huillier, P. Balcou, S. Candel, K. J. Schafer, and K. C. Kulander, *Phys. Rev. A* **46** (1992) 2778
[39] P. Antoine, A. L'Huillier, M. Lewenstein, P. Salie'res, and B. Carr_e, *Phys. Rev. A* **53** (1996) 1725
[40] S. Kazamias, D. Douillet, C. Valentin, F. Weihe, F. Aug_e, Th. Lefrou, G. Grillon, S. Sebban, and Ph. Balcou, *Phys. Rev. A* **68** (2003) 033819
[41] A. Averchi, D. Faccio, R. Berlasso, M. Kolesik, J. V. Moloney, A. Couairon, and P. Di Trapani, *Phys. Rev. A* **77** (2008) 021802
[42] T. Pfeifer, C. Spielmann and G. Gerber, *Rep. Prog. Phys.* **69** (2006) 443
[43] C. G. Durfee, III, A. R. Rundquist, S. Backus, C. Herne, M. M. Murnane, and H. C. Kapteyn, *Phys. Rev. Lett*. **83** (1999) 2187
[44] V. Tosa, E. Takahashi, Y. Nabekawa, and K. Midorikawa, *Phys. Rev. A* **67** (2003) 063817
[45] H. V. Le, K. B. Dinh, P. Hannaford and L. V. Dao, *J. Appl. Phys.* **116** (2014) 173104
[46] H. M. Quiney, *J. Mod. Opt.* **57** (2010) 1109
[47] A. Tripathi J. Mohanty S. H. Dietze O. G. Shpyrko E. Shipton, E. E. Fullerton S. S. Kim, and I. McNulty, *Proc. Natl. Acad. Sci. USA* **108** (2011) 13393
[48] K. B. Dinh, H. V. Le, P. Hannaford and L. V. Dao, *J. Appl. Phys.* **17** (2015) 163102
[49] K. B. Dinh, H. V. Le, P. Hannaford and L. V. Dao, *Opt. Commun.* **396** (2017) 100